Open access • Journal Article • DOI:10.1021/JP804572T

Hierarchically Porous Gd3+-Doped CeO2 Nanostructures for the Remarkable Enhancement of Optical and Magnetic Properties — Source link

Gao-Ren Li, Dun-Lin Qu, Laurent Arurault, Yexiang Tong

Institutions: Sun Yat-sen University

Published on: 05 Jan 2009 - Journal of Physical Chemistry C (American Chemical Society)

Topics: Deposition (chemistry)

Hierarchically Porous Gd^{3+}-Doped CeO_2 Nanostructures for the Remarkable Enhancement of Optical and Magnetic Properties

Gao-Ren Li,*,†,‡ Dun-Lin Qu,† Laurent Arurault,§ and Ye-Xiang Tong*,†

MOE of Key Laboratory of Bioinorganic and Synthetic Chemistry, School of Chemistry and Chemical Engineering, Institute of Optoelectronic and Functional Composite Materials, Sun Yat-Sen University, Guangzhou 510275, China, State Key Laboratory of Rare Earth Materials Chemistry and Applications, Beijing 100871, China, and CIRIMAT-LCMIE, Université Paul Sabatier, 31062 Cedex 9, France

Rare earth ion-doped CeO_2 has attracted more and more attention because of its special electrical, optical, magnetic, or catalytic properties. In this paper, a facile electrochemical deposition route was reported for the direct growth of the porous Gd-doped CeO_2. The formation process of Gd-doped CeO_2 composites was investigated. The obtained deposits were characterized by SEM, EDS, XRD, and XPS. The porous Gd^{3+}-doped CeO_2 (10 at% Gd) displays a typical type I adsorption isotherm and yields a large specific surface area of 135 m^2/g. As Gd^{3+} ions were doped into CeO_2 lattice, the absorption spectrum of Gd^{3+}-doped CeO_2 nanocrystals exhibited a red shift compared with porous CeO_2 nanocrystals and bulk CeO_2, and the luminescence of Gd^{3+}-doped CeO_2 deposits was remarkably enhanced due to the presence of more oxygen vacancies. In addition, the strong magnetic properties of Gd-doped CeO_2 (10 at% Gd) were observed, which may be caused by Gd^{3+} ions or more oxygen defects in deposits. In addition, the catalytic activity of porous Gd-doped CeO_2 toward CO oxidation was studied.

1. Introduction

At present, the synthesis of ceria (CeO_2) nanostructures has aroused much interest because of a wide range of applications such as oxygen gas sensors, solid electrolytes in solid oxide fuel cells, phosphor/luminescence, catalysts for three-way automobile exhaust systems, and ultraviolet absorbers.[1] For some practical applications, the dopants, such as transition and non-transition metal ions, may be introduced into CeO_2 lattices for enhancing its optical properties or increasing its temperature stability and ability to store and release oxygen.[2] Recently attention has been focused on the preparation of rare earth ion-doped CeO_2 because of its special electrical, optical, magnetic or catalytic properties.[3] For instance, the Eu^{3+}(Sm^{3+},Tb^{3+})-doped CeO_2 nanocrystals showed remarkably enhanced photoluminescence (PL) intensity with respect to the CeO_2 nanocrystals due to the increased concentration of oxygen vacancies in the CeO_2 nanocrystals.[4] Gd-doped CeO_2 has shown potential applications in the next generation of compact solid oxide fuel cells for their enhancement in oxygen-exchange processes and associated catalytic reactions.[5]

It is well-known that the performance of ceria-based materials is largely due to the ease in generating Ce^{3+} from Ce^{4+}.[6] In addition, the innate properties of ceria-based materials may be further amplified by producing ceria in nanostructured forms.[7] Therefore, the synthesis of various nanostructures of ceria-based materials and their physical and chemical properties have been widely reported.[8] In the past decade, there has been the tendency toward the development of novel, well-structured, and porous nanostructures, which have the ability to enhance the material properties by increasing the surface-area or providing channels. For example, in the field of solid oxide fuel cells, a porous electrode structure is favorable for a rapid flux of gases through the pores, fast transport of ionic and electronic carriers through the solid phase, and efficient electrochemical reactions at the interfaces. However, at present there are relatively few reports on the preparation and characterization of porous rare earth ion-doped CeO_2 nanostructures.

Various methods, such as hydrothermal synthesis, spray pyrolysis, surfactant-templated synthesis, coprecipitation, and combustion synthesis, have been put forward for the synthesis of diverse CeO_2-based nanomaterials.[9] However, the above methods often required relatively high reaction temperatures (100−1000 °C), special equipment, or multiple reaction steps. In addition, the prepared materials with high specific surface are prone to agglomeration and exhibit broad pore size distributions, including, in some cases, small 1D pores.[10] The process of sintering at high temperature will lead to the loss of surface area and oxygen storage capacity of CeO_2-based materials. Therefore, the preparation of CeO_2-based materials with high specific surface area by the sintering process is still not well-known technology.[11] Here we investigated an electrochemical deposition route for the preparation of hierarchically porous Gd-doped CeO_2 at room temperature, providing a facile and low-cost route for the synthesis of high-quality porous Gd-doped CeO_2 foam nanostructures in high yield. These as-prepared hierarchically porous Gd-doped CeO_2 nanostructures have shown a remarkable enhancement of optical and magnetic properties. In addition, we also have studied catalytic properties of Gd-doped CeO_2.

2. Experimental Section

The electrochemical deposition was carried out in a solution of 0.01 M $Ce(NO_3)_3$−0.01 M $Gd(NO_3)_3$−0.1 M NH_4NO_3. In this experiment a simple three-electrode cell was used in our

* Corresponding author. E-mail: ligaoren@mail.sysu.edu.cn and chedhx@mail.sysu.edu.cn.
† Sun Yat-Sen University.
‡ State Key Laboratory of Rare Earth Materials Chemistry and Applications.
§ Université Paul Sabatier.

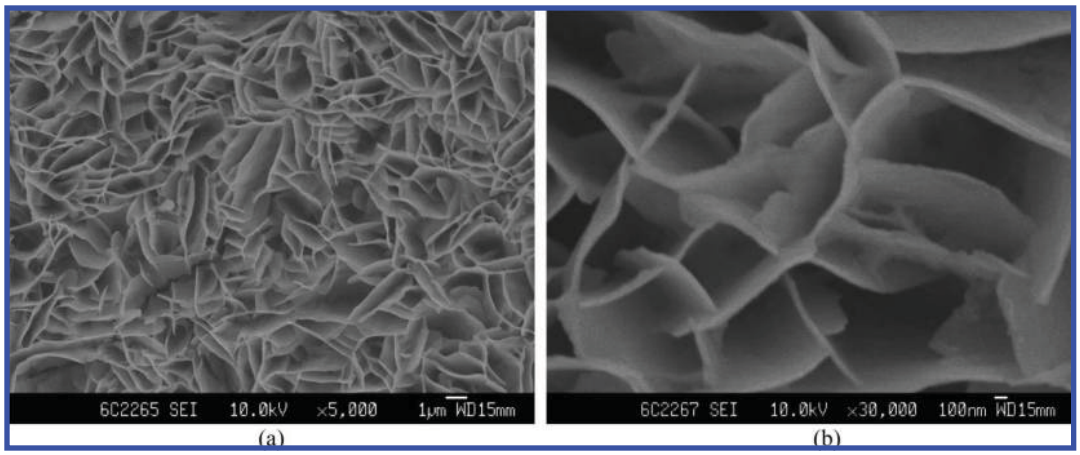

Figure 1. SEM images of porous CeO_2 prepared in a solution of 0.02 mol/L $Ce(NO_3)_3$ + 0.1 mol/L NH_4NO_3 with current density of 1.0 mA/cm^2 with different magnifications: (a) ×5 00; (b) ×30 000.

experiments. A highly pure Pt foil (99.99 wt %, 0.25 cm^2) was used as the auxiliary electrode. A saturated calomel electrode (SCE) was used as the reference electrode that was connected to the cell with a double salt bridge system. All the electrochemical deposition experiments were carried out in a configured glass cell at room temperature, in which a Cu plate (99.99 wt %, 0.5 cm^2) served as the substrate. Before electrodeposition, Cu substrate was cleaned ultrasonically in 0.1 M HCl, distilled water, and acetone and then rinsed in distilled water again. The structures of products were characterized by X-ray diffractometry (D/MAX 2200 VPC with Cu Kα radiation). An Oxford Instrument's INCA energy-dispersive spectrometer (EDS) was employed to analyze chemical composition. Microstructures of the deposits were characterized by field emission scanning electron microscopy (FE-SEM; JSM-6330F). The X-ray photoelectron spectroscopy (XPS, ESCALAB 250) was used to assess the chemical state and surface composition of the deposits.

The UV−vis spectra of the samples were recorded on a UV−vis−NIR spectrophotometer (UV-3150). The photoluminescence (PL) spectra were carried out by spectrofluorophotometer (RF-5301PC) at room temperature. The magnetic property measurement system (MPMS XL-7) was used to investigate the magnetic behaviors of $Ce_{0.9}Gd_{0.1}O_{2-\delta}$ composites. The samples were also characterized by Brunauer, Emmett, and Teller (BET) nitrogen sorption surface area measurements (Micromeritics ASAP 2010). Specific surface areas of the prepared deposits were calculated by the Brunauer−Emmett−Teller (BET) method, and pore sizes were calculated by using the Barrett, Joyner, and Halenda (BJH) method (for large pores) or density functional theory (DFT) method (for small pores) on the basis of the adsorption branch of nitrogen sorption isotherms. Catalytic tests were carried out in a conventional fixed-bed quartz microreactor (8 mm in outer diameter) at atmospheric pressure. The system was first purged with high-purity N_2 gas (40 mL min^{-1}) and then a gas mixture of $CO/O_2/N_2$ (1:20:79) was introduced into the reactor, which contained 40-mg samples at a flow rate of 40 mL min^{-1}. Gas samples were analyzed by an online gas chromatography, using a Porapak Q column for the separation of CO_2 and CO and a 5A Molecular Sieve column for the separation of N_2 and O_2. The catalytic performance was evaluated at various temperatures.

3. Results and Discussion

Figure 1 shows the SEM images of the CeO_2 deposits prepared in a solution of 0.02 M $Ce(NO_3)_3$−0.1 M NH_4NO_3 with current density of 1.0 mA/cm^2. The porous CeO_2 foam structures were successfully prepared. The thickness of walls is about 50 nm as shown in Figure 1b. The sizes of pores are between 3 and 8 μm. The porous structures of the deposits can be manipulated by adding $Gd(NO_3)_3$ into deposition solution. When the electrodeposition was carried out in a solution of 0.01 M $Ce(NO_3)_3$−0.01 M $Gd(NO_3)_3$−0.10 M NH_4NO_3 with a current density of 1.0 mA/cm^2, the porous Gd-doped CeO_2 foam structures were prepared, and the SEM images were shown in Figure 2. It can be easily found that the foam structures have a higher density of pores, and the sizes of pores are smaller, which are about 200−500 nm.

EDS measurement was carried out at a number of locations throughout the specimens, and a representative EDS pattern of porous Gd-doped CeO_2 foam structure was shown in Figure 3. An oxygen peak at about 0.5 keV and Ce signals at about 0.9, 4.9, and 6.0 keV were observed, respectively. The Gd peaks at 0.9, 6.0, and 8.1 keV were observed. The EDS results therefore demonstrated that O, Ce, and Gd were electrodeposited. The composition analysis showed an approximate atom ratio of Ce to Gd was about 9:1 in the Gd-doped CeO_2 composites. For the element Ce, there are two different oxidation states Ce^{3+} and Ce^{4+}. The Ce^{4+} oxidation state is more stable than Ce^{3+} in the presence of air. It is well-known that there coexists a small amount of Ce^{3+} at the surface of CeO_2.[12] The results of XPS analyses of Gd-doped CeO_2 deposits (10 atom % Gd) were shown in Figure 4. The presence of Ce^{3+} ions in the CeO_2 nanocrystals has been confirmed by XPS analysis, with Ce^{3+} peaks found at 883 and 901 eV in Figure 4a(1). The binding energies of Ce^{3+} ions in Gd-doped CeO_2 deposits are red-shifted compared to bulk CeO_2.[13] The XPS peaks centered at 1188 and 1219 eV in Figure 4b can be attributed to the Gd^{3+} contribution. In addition, the XPS peak centered at 529.3 eV in Figure 4c can be attributed to the O^{2-} contribution.[14] Therefore, the XPS results demonstrated the obtained deposits were Gd^{3+}-doped CeO_2 with a small quantity of Ce^{3+} oxidation state. The XPS spectrum of porous Gd-doped CeO_2 deposits (12 atom % Gd) was shown in Figure 4a(2). Although the peaks of Ce^{4+} in Figure 4a(2) are almost the same as those in Figure 4a(1), the peaks of Ce^{3+} in Figure 4a(2) are obviously lower than those in Figure 4a(1), indicating the variation of Ce(III)/Ce(IV) ratios.

The formation process of Gd-doped CeO_2 composites (10 atom % Gd) was investigated as follows. During the electrodeposition, OH^- ions were formed via the electroreduction of NO_3^- ions in deposition solution on the surface of the cathode. These produced OH^- ions will result in the formation

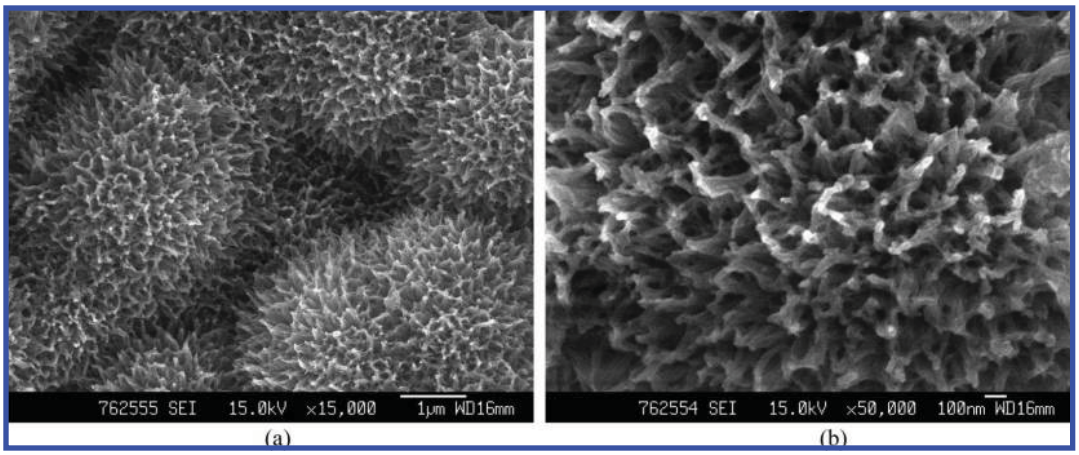

Figure 2. SEM images of porous Gd-doped CeO_2 prepared in a solution of 0.01 M $Ce(NO_3)_3$−0.01 M $Gd(NO_3)_3$−0.1 M NH_4NO_3 with current density of 1.0 mA/cm^2: (a) ×15 000; (b) ×50 000.

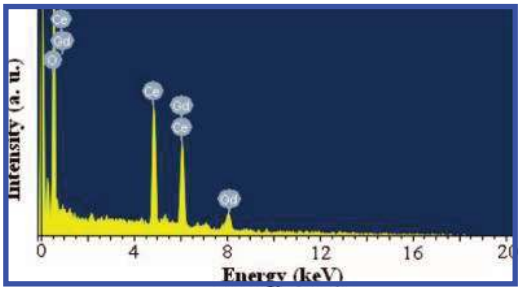

Figure 3. EDS pattern of the porous Gd-doped CeO_2 composite foam structures.

of CeO_2 and Gd_2O_3, and the formation processes of CeO_2 and Gd_2O_3 can be expressed as eqs 1, 2, and 3. It is well-known that the electrochemical deposition allows mixing of the chemicals at the atomic level. Therefore, when the electrodeposition was carried out, the mixed CeO_2 and Gd_2O_3 at the atomic level were always obtained, and accordingly the homogeneous Gd-doped CeO_2 composites were prepared (eq 4).

$$NO_3^- + H_2O + 2e \rightarrow NO_2^- + 2OH^- \quad (1)$$

$$2Gd^{3+} + 6OH^- \rightarrow Gd_2O_3 + 3H_2O \quad (2)$$

$$4Ce^{3+} + 12OH^- + O_2 \rightarrow 4CeO_2 + 6H_2O \quad (3)$$

$$Gd_2O_3 + 18CeO_2 \rightarrow 20Ce_{0.9}Gd_{0.1}O_{2-\delta} \quad (4)$$

Further characterization by X-ray powder diffraction was carried out, and the XRD patterns of CeO_2 (a) and Gd^{3+}-doped CeO_2 (10 atom % Gd) (b) porous structures were shown in Figure 5. The results of XRD indicate that the CeO_2 nanocrystals are well-crystallized. The peaks corresponding to the CeO_2 (111), (200), (220), and (311) planes were observed, and all these diffraction peaks of CeO_2 can be indexed as a face-centered cubic-phase as identified by using the standard data JCPDS 34-0394. Here, we should notice that the XRD peaks of CeO_2 in the 2θ range from 25° to 70° exhibit the broadened peaks with a little shift toward smaller angles. According to the Scherrer equation (i.e., $D = K\lambda/(\beta \cos\theta)$ (where λ is the wavelength of the X-ray radiation, K is a constant taken as 0.89, θ is the diffraction angle, and β is the full width at half-maximum), the strongest peak (111) at $2\theta = 28.8°$ and the peak (220) at $2\theta = 47.4°$ were used to calculate the average crystallite size of CeO_2 nanocrystals, determined to be around 5.0 nm. The cell parameter (a) is calculated as about 0.5441 nm, a little larger than that of bulk CeO_2 (0.5411 nm). The larger cell parameter may be attributed to the lattice expansion effect resulting from the increased Ce^{3+} ions and oxygen vacancies.[15] For Gd^{3+}-doped CeO_2 porous structures, the XRD pattern in Figure 5b was almost the same as that of CeO_2 porous structures, and all diffraction peaks can be indexed to the face-centered cubic-phase of CeO_2. The average crystal size of Gd^{3+}-doped CeO_2 nanocrystals was estimated as about 4.5 nm by the Scherrer equation. However, the diffraction peaks of Gd or Gd_2O_3 were not observed in the XRD pattern, indicating Gd^{3+} ions entering into CeO_2 lattices. The cell parameter values were calculated as about 0.5429 nm, which is a little smaller than that of porous CeO_2. This may be due to the lattice constriction effect resulting from Gd^{3+} ions. This can be attributed to the replacement of Ce^{3+} by trivalent Gd^{3+} ions. As we all know, the ionic radius of Gd^{3+} (107.8 pm) is smaller than those of Ce^{3+} (115 pm). Therefore, the lattice constricts upon Gd^{3+} doping will happen.

The porous CeO_2 and Gd^{3+}-doped CeO_2 (10 atom % Gd) have been studied by the Raman scattering method as shown in Figure 6. For the porous CeO_2, one high and sharp peak at 461 cm^{-1} is clearly observed in Figure 6a, which can be assigned to $F2g$ symmetry because of a symmetric breathing mode of the oxygen atoms around the cerium ions.[16,17] The Raman shift is about 3 cm^{-1} compared with the bulk CeO_2 (464 cm^{-1}). It is well-known that the change of the Raman peak′s position can be attributed to the changes of bond length or lattice spacing. For porous CeO_2, the shift of the Raman peak is related to the enlarged lattice space because of the smaller size of CeO_2 crystals (5.0 nm).[18−20] In addition, the Raman shift also can be calculated by the following equation:[16]

$$\Delta\omega = -3\gamma\omega_0\Delta a/a_0 \quad (5)$$

where γ is the Grüneisen constant, ω_0 is the Raman frequency of bulk CeO_2, Δa is the change in lattice constant, and a_0 is the lattice constant of bulk CeO_2 (0.5411 nm). The Raman frequency shift $\Delta\omega$ can be calculated as about −3.32 cm^{-1}, which is very close to the above experimental value. However, for the porous Gd^{3+}-doped CeO_2, the first-order peak was shifted to 456 cm^{-1}, and this peak became broad compared with that of porous CeO_2. For porous Gd^{3+}-doped CeO_2, the shift of the Raman peak is also related to the change in lattice spacing caused by the constriction of the lattice upon Gd-doping and to the change in the atomic geometry arising from Gd-doping. These lead to a larger shift compared with the porous CeO_2. In addition, one weak peak at about 602 cm^{-1} was observed, which could be associated with the presence of the Gd element.

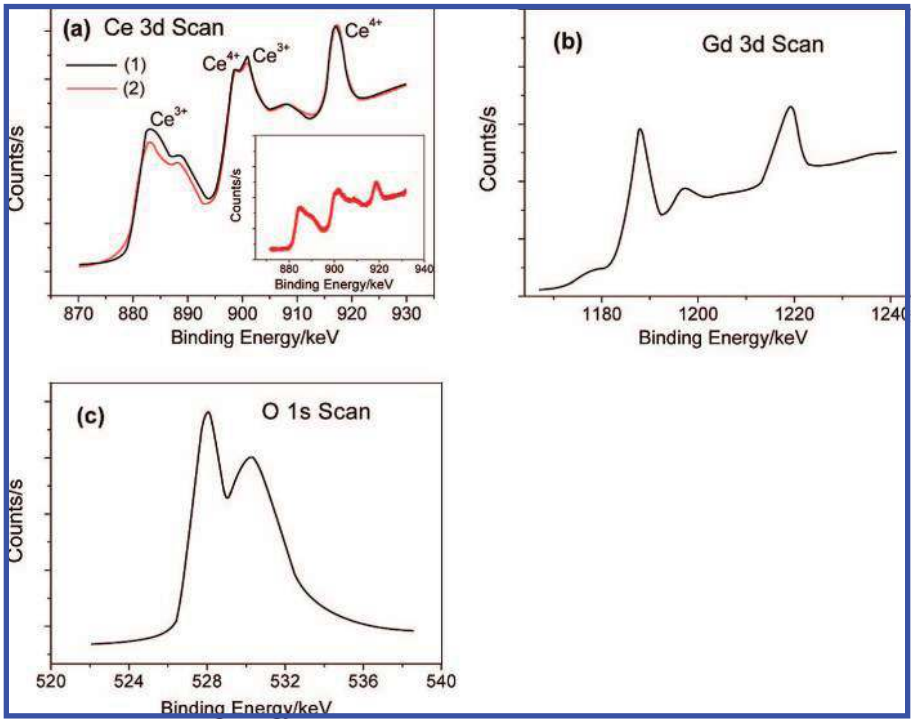

Figure 4. XPS spectra of Gd-doped CeO_2: (a) Ce 3d in $Ce_{0.9}Gd_{0.1}O_{2-\delta}$ (1); Ce 3d in $Ce_{0.88}Gd_{0.12}O_{2-\delta}$ (2); Ce 3d of porous CeO_2 (inset); (b) Gd 3d; and (c) O1s spectra in $Ce_{0.9}Gd_{0.1}O_{2-\delta}$.

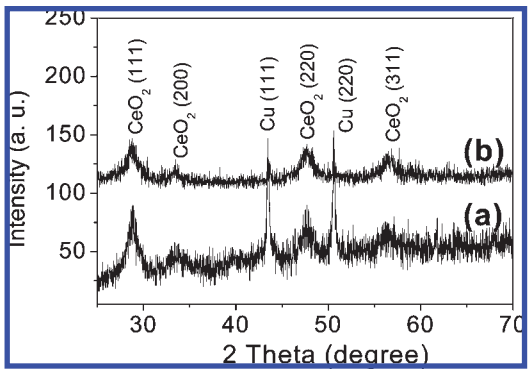

Figure 5. XRD patterns of (a) Gd-doped CeO_2 (10 atom % Gd) and (b) CeO_2 porous structures.

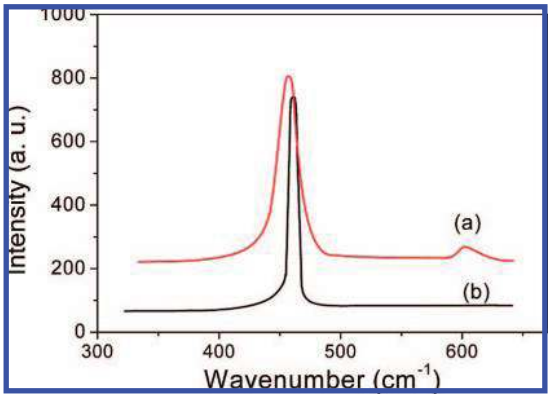

Figure 6. Raman spectra of (a) Gd-doped CeO_2 (10 atom % Gd) and (b) CeO_2 porous structures taken at room temperature.

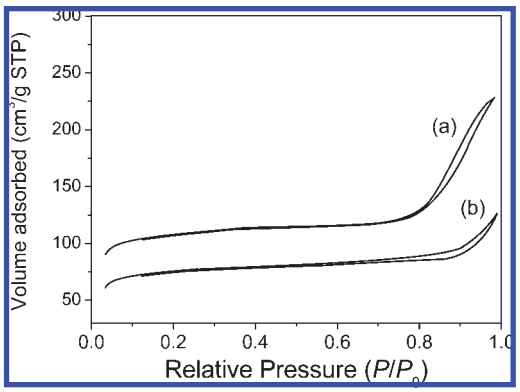

Figure 7. N_2 adsorption−desorption isotherms of (a) Gd-doped CeO_2 (10 atom % Gd) and (b) CeO_2 porous structures.

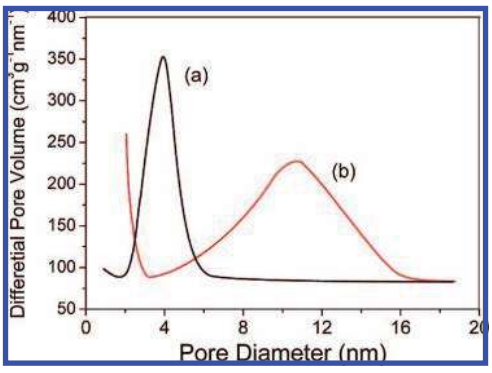

Figure 8. DFT pore size distributions of (a) Gd-doped CeO_2 (10 atom % Gd) and (b) CeO_2 porous structures.

The porosity of the synthesized porous CeO_2 and Gd^{3+}-doped CeO_2 (10 atom % Gd) were characterized by nitrogen sorption analysis, using standard Brunauer−Emmett−Teller (BET) techniques. The nitrogen adsorption and desorption isotherms and the resulting pore size distributions of porous CeO_2 and Gd^{3+}-doped CeO_2 are shown in Figures 7 and 8, respectively. The porous CeO_2 and Gd^{3+}-doped CeO_2 both display a typical type I adsorption isotherm and yield specific surface areas of 93 and 135 m^2/g, respectively. Thus, the specific surface area of porous Gd^{3+}-doped CeO_2 was larger than that of porous CeO_2. The pore diameters of porous Gd^{3+}-doped CeO_2 and CeO_2 are

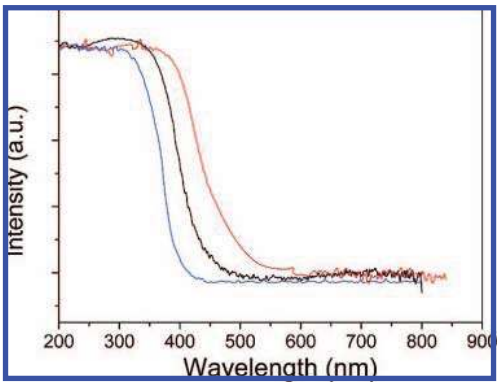

Figure 9. UV−vis absorption spectra of porous Gd-doped CeO_2 (10 atom % Gd) (red line), porous CeO_2 (blue line), and bulk CeO_2 (black line).

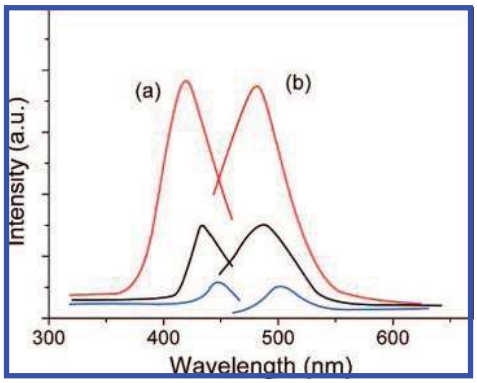

Figure 10. Excitation (a) and emission (b) spectra of porous Gd-doped CeO_2 (10 atom % Gd) (red line), porous CeO_2 (black line), and bulk CeO_2 (blue line) in hexane solution.

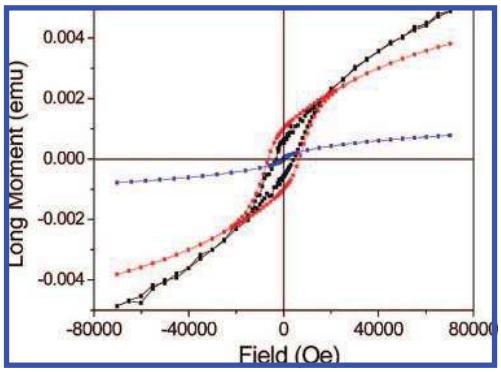

Figure 11. The magnetization hysteresis loops of porous Gd-doped CeO_2 (10 atom % Gd) (red line), porous CeO_2 (black line), and bulk CeO_2 (blue line) at 5 K.

distributed with peaks centered at around 4 and 11 nm, respectively.

For the porous CeO_2, there is a strong absorption band below 400 nm in the spectrum as shown in Figure 9, which is due to the charge-transfer transition from O^{2-} (2p) to Ce^{4+} (4f) orbitals in CeO_2.[21] However, the absorption spectrum of Gd^{3+}-doped CeO_2 (10 atom % Gd) nanocrystals exhibits a red shift compared with porous CeO_2 nanocrystals and bulk CeO_2. For CeO_2 nanocrystals, it is well-known that there coexists a small amount of Ce^{3+} at the surface of CeO_2 and the fraction of Ce^{3+} ions increases with decreasing particle size.[22,23] The presence of Ce^{3+} ions in the CeO_2 nanocrystals can be confirmed by XPS analysis as shown in Figure 4a. The valence change from Ce^{4+} to Ce^{3+} on the surface of nanocrystals might have some additional contributions to the absorption of CeO_2 nanocrystals because the change from +4 to +3 increases the charge-transfer gap between O 2p and Ce 4f bands, which leads to the blue-shift of absorption spectrum of CeO_2 nanocrystals compared with bulk CeO_2.[24] In addition, the average size of the obtained Gd^{3+}-doped CeO_2 nanocrystals is about 5.0 nm, which is smaller than the estimated exciton Bohr radius for CeO_2 (7−8 nm).[25] Therefore, a quantum confinement effect possibly takes place, which contributes to the blue-shift of the absorption edge of the porous CeO_2. When Gd^{3+} was doped into CeO_2, the peaks of Ce^{4+} $3d_{3/2}$ and Ce^{4+} $3d_{5/2}$ become stronger than that of the undoped CeO_2 nanocrystals as shown in the XPS spectrum in the inset in Figure 4a, while those of Ce^{3+} $3d_{3/2}$ and Ce^{3+} $3d_{5/2}$ are relatively weak, indicating the decrease of the Ce^{3+} fraction on the surface of CeO_2. This may be attributed to the replacement of Ce^{3+} by trivalent Gd^{3+} ions. Accordingly, the contribution of blue-shifting arising from the Ce^{4+} to Ce^{3+} valence change will become small. Therefore, the red-shifting occurs in the absorption spectrum of Gd^{3+}-doped CeO_2 (10 atom % Gd) nanocrystals compared with that of CeO_2 nanocrystals. According to eq 6, the optical band gaps (E_g) of porous CeO_2 and Gd^{3+}-doped CeO_2 can be estimated by using the data for the absorption spectra:

$$ahv = C(hv - E_g)^n \quad (6)$$

Here hv is photon energy, α is the absorption coefficient, C is the constant, $n = 2$ for an indirectly allowed transition, and $n = 1/2$ for a directly allowed transition.[26] The direct band gap values of porous CeO_2 and Gd^{3+}-doped CeO_2 nanocrystals can be determined as about 3.10 and 2.48 eV, respectively.

The photoluminescent (PL) properties of porous CeO_2 and Gd^{3+}-doped CeO_2 (10 atom % Gd) were also investigated. Figure 10 shows the excitation (a) and emission (b) spectra of porous Gd^{3+}-doped CeO_2 (red lines) and CeO_2 (black lines). The band emission of CeO_2 can be remarkably enhanced by doping Gd^{3+} into CeO_2 lattices. According to the above results, the emissions of CeO_2 and Gd^{3+} were not detected in the Gd^{3+}-doped CeO_2, and the luminescence spectra shown in Figure 10 are from oxygen vacancies.[4] The extrinsic oxygen vacancies are generated in the fluorite lattice of CeO_2 nanocrystals because of the existence of Ce^{3+}.[4] When Gd^{3+} ions are doped into CeO_2 nanocrystals, the fraction of trivalent Ce^{3+} ions will be decreased because of the replacement of Ce^{3+} by Gd^{3+} ions; however, the oxygen vacancy concentration in CeO_2:Gd^{3+} nanocrystals must be much higher because the doping concentration of Gd^{3+} is much larger than the fraction of Ce^{3+} in undoped nanocrystals.[4] Therefore, when Gd^{3+} ions were doped into CeO_2 lattice, the enhancement of luminescence of Gd^{3+}-doped CeO_2 deposits is attributed to the increase of oxygen vacancies.

Figure 11 shows the magnetization hysteresis loops of porous CeO_2 and Gd^{3+}-doped CeO_2 (10 atom % Gd) at 5 K. As we all know, the stoichiometric CeO_2 should be nonmagnetic. However, the obvious magnetic property was observed for the prepared porous CeO_2 and Gd-doped CeO_2. The coercivity field (H_c) and the remanent magnetization (M_r) of Gd-doped CeO_2 were larger than those of porous CeO_2. For porous Gd^{3+}-doped CeO_2, the H_c is about 6838 Oe, and M_r is about 1.02×10^{-3} emu at 5 K. What leads to the stronger magnetic property of the porous Gd^{3+}-doped CeO_2? The mechanism of the origin of magnetism in doped CeO_2 is still under investigation. It has been proved that the oxygen defects and Ce^{3+} ions existed in porous CeO_2 deposits by XRD and XPS, and the Ce^{3+} ions in deposits can lead to the magnetic properties of CeO_2.[13b,27]

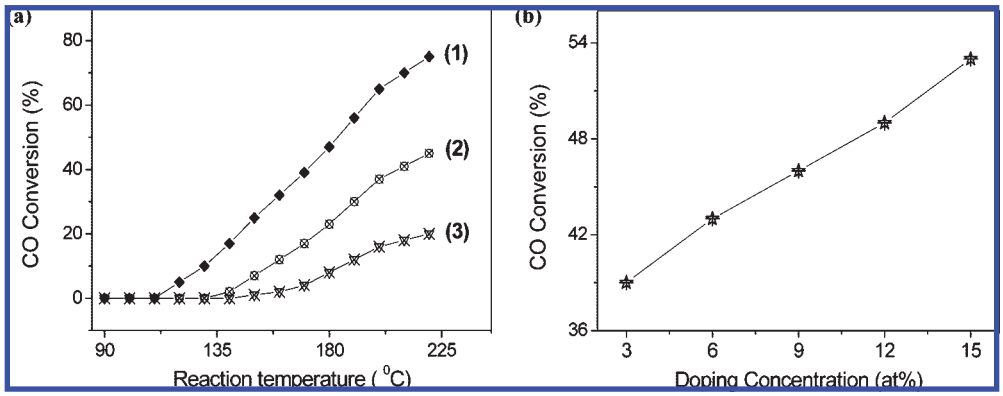

Figure 12. (a) CO conversion as a function of temperature for the as-deposited porous Gd-doped CeO_2 (10 atom % Gd) (1), porous CeO_2 (2), and CeO_2 nanoparticles (3). (b) CO conversion as a function of doping concentration for the as-deposited porous Gd-doped CeO_2 at 180 °C.

Therefore, the stronger magnetic properties of Gd-doped CeO_2 may be caused by the higher concentration of Gd^{3+} ions in deposits.

CeO_2 is an important three-way catalyst, and we studied the catalytic activity of porous Gd-doped CeO_2 (10 at% Gd), porous CeO_2, and CeO_2 nanoparticles. Catalytic activities of CeO_2 samples as a function of reaction temperature are shown in Figure 12a. The CO conversion increases with increasing reaction temperature for all samples. It can be clearly observed that porous Gd-doped CeO_2 shows much higher activity than porous CeO_2 and CeO_2 nanoparticles. For porous Gd-doped CeO_2, a 47% CO conversion is achieved at 180 °C, while only 23% and 8% CO conversions are obtained at the same temperature for porous CeO_2 and CeO_2 nanoparticles, respectively. For the same CO conversion (20%), the reaction temperature for porous Gd-doped CeO_2 can be 30 and 76 °C lower than those for porous CeO_2 and CeO_2 nanoparticles, respectively. The large difference in catalytic activity can be partly due to the variation in surface area. It is well-known that the catalytic process is mainly related to the adsorption and desorption of gas molecules on the surface of catalyst.[28] Therefore, the porous structures with high surface area enable better contact with gas molecules, and accordingly show better catalytic performance compared with CeO_2 nanoparticles. In addition to the surface area, the oxygen vacancies in CeO_2 are also an important factor for better performance as they can act as promoting sites for CO conversion.[1d] On the basis of the above results, the oxygen vacancy concentration in porous Gd-doped CeO_2 is much larger than those of porous CeO_2 and CeO_2 nanoparticles, which further promotes the catalytic performance of porous Gd-doped CeO_2. Figure 12b shows CO conversion as a function of doping concentration for the as-deposited porous Gd-doped CeO_2 at 180 °C, indicating oxidation ability increases with doping concentration.

4. Conclusions

In summary, a facile electrochemical deposition route was developed for the direct growth of porous Gd-doped CeO_2. The porous Gd^{3+}-doped CeO_2 (10 atom % Gd) displays a typical type I adsorption isotherm and yields a specific surface area of 135 m^2/g. The pore diameters of porous Gd^{3+}-doped CeO_2 (10 atom % Gd) are distributed with peaks centered at around 4 nm. The XPS results demonstrated the obtained Gd^{3+}-doped CeO_2 deposits have a small quantity of Ce^{3+} oxidation state. The optical band gap values of porous Gd^{3+}-doped CeO_2 (10 atom % Gd) nanocrystals can be determined as 2.48 eV, which is much smaller than 3.10 eV of porous CeO_2. In addition, when Gd^{3+} ions were doped into CeO_2 lattice, the luminescence of Gd^{3+}-doped CeO_2 deposits was remarkably enhanced, which can be attributed to the rapid oxygen vacancy increase. The magnetic properties of porous CeO_2 may be caused by the Ce^{3+} ions in deposits, and the stronger magnetic properties of Gd-doped CeO_2 were caused by more RE^{3+} ions in deposits. Furthermore, better catalytic actives of porous Gd^{3+}-doped CeO_2 nanocrystals were obtained compared with those of porous CeO_2 and CeO_2 nanoparticles.

Acknowledgment. This work was supported by the Natural Science Foundation of China (Grant No. 20603048 and 20873184), the Guangdong Province Science & Technology Development Program (2008B010600040), and the Foundation of Potentially Important Natural Science Research of Sun Yat-Sen University.

References and Notes

(1) (a) Nolan, M.; Watson, G. W. *J. Phys. Chem. B* **2006**, *110*, 2256. (b) Nolan, M.; Watson, G. W. *J. Phys. Chem. B* **2006**, *110*, 16600. (c) Feng, X.; Sayle, D. C.; Wang, Z. L.; Paras, M. S.; Santora, B.; Sutorik, A. C.; Sayle, T. X. T.; Yang, Y.; Ding, Y.; Wang, X. D.; Her, Y. S. *Science* **2006**, *312*, 1504–1508. (d) Ho, C.; Yu, J. C.; Kwong, T.; Mak, A. C.; Lai, S. *Chem. Mater.* **2005**, *17*, 4514–4522. (e) Tarnuzzer, R. W.; Colon, J.; Patil, S.; Seal, S. *Nano Lett.* **2005**, *5*, 2573. (f) Leah, R. T.; Brandon, N. P.; Aguiar, P. *J. Power Sources* **2005**, *145*, 336. (g) Morshed, A. H.; Moussa, M. E.; Bedair, S. M.; Leonard, R.; Liu, S. X.; El-Masry, N. *Appl. Phys. Lett.* **1997**, *70*, 1647. (h) Laha, S. C.; Ryoo, R. *Chem. Commun.* **2003**, 2138.

(2) (a) Matolin, V.; Sedlacek, L.; Matolinova, I.; Sutara, F.; Skala, T.; Smid, B.; Libra, J.; Nehasil, V.; Prince, K. C *J. Phys. Chem. C* **2008**, *112*, 3751–3758. (b) Romero-Sarria, F.; Martinez, T., L. M.; Centeno, M. A.; Odriozola, J. A. *J. Phys. Chem. C* **2007**, *111*, 14469–14475. (c) Reddy, B. M.; Bharali, P.; Saikia, P.; Khan, A.; Loridant, S.; Muhler, M.; Grunert, W. *J. Phys. Chem. C* **2007**, *111*, 1878–1881. (d) Perkas, N.; Rotter, H.; Vradman, L.; Landau, M. V.; Gedanken, A. *Langmuir* **2006**, *22*, 7072–7077. (e) Li, G.; Mao, Y.; Li, L.; Feng, S.; Wang, M.; Yao, X. *Chem. Mater.* **1999**, *11*, 1259–1266. (f) Abimanyu, H.; Ahn, B. S.; Kim, C. S.; Yoo, K. S. *Ind. Eng. Chem. Res.* **2007**, *46*, 7936–7941. (g) de Carolis, S.; Pascual, J. L.; Pettersson, L. G. M.; Baudin, M.; Wojcik, M.; Hermansson, K.; Palmqvist, A. E. C.; Muhammed, M. *J. Phys. Chem. B* **1999**, *103*, 7627–7636.

(3) (a) Linares, R. C. *J. Opt. Soc. Am.* **1966**, *56*, 1700. (b) Yugami, H.; Nakajima, A.; Ishigame, M.; Suemoto, T. *Phys. Rev. B* **1991**, *44*, 4862. (c) Fujihara, S.; Oikawa, M. *J. Appl. Phys.* **2004**, *95*, 8002. (d) Maher, R. C.; Cohen, L. F.; Lohsoontorn, P.; Brett, D. J. L.; Brandon, N. P. *J. Phys. Chem. A* **2008**, *112*, 1497–1501. (e) Suzuki, T.; Kosacki, I.; Petrovsky, V.; Anderson, H. U. *J. Appl. Phys.* **2002**, *91*, 2308–2313. (f) Rupp, J. L. M.; Drobek, T.; Rossi, A.; Gauckler, L. J. *Chem. Mater.* **2007**, *19*, 1134–1142.

(4) Wang, Z.; Quan, Z.; Lin, J. *Inorg. Chem.* **2007**, *46*, 5237–5242.

(5) (a) Sahibzada, M.; Steele, B. C. H.; Zheng, K.; Rudkin, R. A.; Metcalfe, I. S. *Catal. Today* **1997**, *38*, 459. (b) Perez-Coll, D.; Nunez, P.; Ruiz.Morales, J. C.; Pena-Martinez, J.; Frade, J. R. *Electrochim. Acta* **2007**, *52*, 2001. (c) Popovic, Z. V.; Dohcevic-Mitrovic, Z.; Konstantinovic, M. J.; Scepanovic, M. J. *Raman Spectrosc.* **2007**, *38*, 750.

(6) Tschöpe, A. *J. Electroceram.* **2005**, *14*, 5–23.

(7) Laberty-Robert, C.; Long, J. W.; Lucas, E. M.; Pettigrew, K. A.; Stroud, R. M.; Doescher, M. S.; Rolison, D. R. *Chem. Mater.* **2006**, *18*, 50–58.

(8) (a) Ahniyaz, A.; Sakamoto, Y.; Bergström, L. *Cryst. Growth Des.* **2008**, *8*, 1798–1800. (b) Du, N.; Zhang, H.; Chen, B.; Ma, X.; Yang, D. *J. Phys. Chem. C* **2007**, *111*, 12677–12680. (c) Liang, X.; Wang, X.; Zhuang, Y.; Xu, B.; Kuang, S.; Li, Y. *J. Am. Chem. Soc.* **2008**, *130*, 2736–2737. (d) Natile, M. M.; Glisenti, A. *Chem. Mater.* **2005**, *17*, 3403–3414. (e) Ahniyaz, A.; Sakamoto, Y.; Bergström, L. *Cryst. Growth Des.* **2008**, *8*, 1798–1800. (f) Du, N.; Zhang, H.; Chen, B.; Ma, X.; Yang, D. *J. Phys. Chem. C* **2007**, *111*, 12677–12680. (g) Liang, X.; Wang, X.; Zhuang, Y.; Xu, B.; Kuang, S.; Li, Y. *J. Am. Chem. Soc.* **2008**, *130*, 2736–2737. (h) Natile, M. M.; Glisenti, A. *Chem. Mater.* **2005**, *17*, 3403–3414.

(9) (a) Hirano, M.; Kato, E. *J. Am. Ceram. Soc.* **1996**, *79*, 777–780. (b) Gesser, H. D.; Goswami, P. C. *Chem. Rev.* **1989**, *89*, 765–788. (c) Masui, T.; Fujiwara, K.; Machida, K.; Adachi, G.; Sakata, T.; Mori, H. *Chem. Mater.* **1997**, *9*, 2197–2204. (d) Pijolat, M.; Viricelle, J. P.; Sosutelle, M. *Stud. Surf. Sci. Catal.* **1997**, *91*, 885–891. (e) Purohit, R. D.; Sharma, D.; Pillai, K. T.; Tyagi, A. K. *Mater. Res. Bull.* **2001**, *36*, 2711–2716.

(10) Laberty-Robert, C.; Long, J. W.; Pettigrew, K. A.; Stroud, R. M.; Rolison, D. R. *Adv. Mater.* **2007**, *19*, 1734–1739.

(11) Yuzhakova, T.; Rakić, V.; Guimon, C.; Auroux, A. *Chem. Mater.* **2007**, *19*, 2970–2981.

(12) Tsunekawa, S.; Fukuda, T.; Kasuya, A. *Surf. Sci.* **2000**, *457*, L437.

(13) (a) Bumajdad, A.; Zaki, M. I.; Eastoe, J.; Pasupulety, L. *Langmuir* **2004**, *20*, 11223–11233. (b) Li, G.-R.; Qu, D.-L.; Yu, X.-L.; Tong, Y.-X. *Langmuir* **2008**, *24*, 4254–4259.

(14) (a) Salvi, A. M.; Decker, F.; Varsano, F.; Speranza, G. *Surf. Interface Anal.* **2001**, *31*, 255. (b) Huang, P. X.; Wu, F.; Zhu, B. L.; Gao, X. P.; Zhu, H. Y.; Yan, T. Y.; Huang, W. P.; Wu, S. H.; Song, D. Y. *J. Phys. Chem. B* **2005**, *109*, 19169–19174.

(15) (a) Tsunekawa, S.; Sahara, R.; Kawazoe, Y.; Ishikawa, K. *Appl. Surf. Sci.* **1999**, *152*, 53. (b) Tsunekawa, S.; Ishikawa, K.; Li, Z. Q.; Kawazoe, Y.; Kasuya, A. *Phys. Rev. Lett.* **2000**, *85*, 3440. (c) Zhou, X.-D.; Huebner, W. *Appl. Phys. Lett.* **2001**, *79*, 3512. (d) Wu, L. J.; Wiesmann, H. J.; Moodenbaugh, A. R.; Klie, R. F.; Zhu, Y.; Welch, D. O.; Suenaga, M. *Phys. Rev. B* **2004**, *69*, 125415.

(16) McBride, J. R.; Hass, K. C.; Poindexter, B. D.; Weber, W. H. *J. Appl. Phys.* **1994**, *76*, 2435.

(17) Li, X. M; Li, L. P; Li, G. S.; Su, W. H *Mater. Chem. Phys.* **2001**, *69*, 236.

(18) Spanier, J. E.; Robinson, R. D.; Zhang, F.; Chan, S. W.; Herman, I. P. *Phys. Rev. B* **2001**, *64*, 245407.

(19) Weber, W. H.; Hass, K. C.; McBride, J. R. *Phys. Rev. B* **1993**, *48*, 178.

(20) Graham, G. W.; Weber, W. H.; Peters, C. R.; Usmen, R. *J. Catal.* **1991**, *130*, 310.

(21) Zhang, Y. W.; Si, R.; Liao, C. S.; Yan, C. H.; Xiao, C. X.; Kou, Y. *J. Phys. Chem. B* **2003**, *107*, 10159.

(22) Wu, L. J.; Wiesmann, H. J.; Moodenbaugh, A. R.; Klie, R. F.; Zhu, Y.; Welch, D. O.; Suenaga, M. *Phys. Rev. B* **2004**, *69*, 125415.

(23) Tsunekawa, S.; Fukuda, T.; Kasuya, A. *Surf. Sci.* **2000**, *457*, L437.

(24) Tsunekawa, S.; Fukuda, T.; Kasuya, A. *J. Appl. Phys.* **2000**, *87*, 1318.

(25) Tsunekawa, S.; Wang, J.-T.; Kawazoe, Y. *J. Alloys Compd.* **2006**, *408−412*, 1145.

(26) Yin, L.; Wang, X. Y. Q.; Pang, G. S.; Koltypin, Y.; Gedanken, A. *J. Colloid Interface Sci.* **2002**, *246*, 78.

(27) Li, G.-R.; Qu, D.-L.; Tong, Y.-X. *Electrochem. Commun.* **2008**, *10*, 80–84.

(28) Chen, G.; Xu, C.; Song, X.; Zhao, W.; Ding, Y.; Sun, S. *Inorg. Chem.* **2008**, *47*, 723–728.

JP804572T